Independent Electromagnetic Field Control for Practical Approach to Actively Locomotive Wireless Capsule Endoscope

Manh Cuong Hoang, Kim Tien Nguyen, Viet Ha Le, Jayoung Kim, Eunpyo Choi, Byungjeon Kang, Jong-Oh Park, *Member, IEEE*, and Chang-Sei Kim, *Member, IEEE*

***Abstract*—Toward wireless medical microrobot applications driven by an electromagnetic actuation (EMA) system, challenges associated with movability, the electromagnetic force, and the coil system size must be addressed. This paper presents an enhanced EMA system with a higher magnetic field via new coil configurations, an independent magnetic field control method, and application to the multi-degree-of-freedom (DOF) motion of an untethered capsule endoscope. The magnetically actuated capsule endoscope (MACE) system proposed herein consists of an endoscopic capsule with a permanent magnet in the body, eight air-cored stationary electromagnetic coils, and a control system. The coil system is designed to maximize the working space available within a limited equipment space. The MACE is designed to perform full 5-DOF motion, including 3-DOF translation and 2-DOF rotation. The independent magnetic field control method with the new coil configuration enables orientation-independent-driving (OID) control of the capsule endoscope that could not be accomplished by previous EMA systems. The developed system performance was verified by simulations and experiments. The MACE motion in the spatial domain was evaluated with a robotic endoscopic procedure and diagnostic performance by *in-vitro* and *ex-vivo* experiments.**

***Index Terms*—Capsule endoscope, electromagnetic actuation (EMA) system, independent magnetic field control, medical microrobotics.**

TABLE I
ACRONYMS AND ABBREVIATIONS

ALICE	Active locomotion intestinal capsule endoscope
DOF	Degree-of-freedom
EMA	Electromagnetic actuation
FEM	Finite Element Method
HAG	Head-and-Go
HC	Helmholtz coil
MACE	Magnetically actuated capsule endoscope
MC	Maxwell coil
MGCE	Magnetic guided capsule endoscope
OID	Orientation-independent-driving
RC	Rectangular coil
ROI	Region of interest
WCE	Wireless capsule endoscope

I. INTRODUCTION

THE FIRST wireless capsule endoscope (WCE) (Table I summarizes the acronyms and abbreviations used in this paper) in 2000 triggered a revolution in wireless noninvasive diagnosis methods for the gastrointestinal tract in the medical field [1]–[3]. A camera-equipped pill-size capsule is swallowed through the mouth, and it is used to visualize the digestive organs by transmitting captured images to a clinician for further diagnosis [4]–[6], providing a comfortable and convenient untethered gastrointestinal tract diagnosis methodology [7]. However, passive movement and limited operation time and space have been the major drawbacks of the first-generation WCEs [8], [9]. Because it does not have active locomotion, a WCE moves passively by the peristalsis motions of the digestive organs, and thus, the conventional capsule cannot perform endoscopic motion that is controlled by a clinician, especially in large-volume organs, such as the stomach, and folding structures, like the colon. Therefore, it is necessary to integrate active locomotion of the capsule so that a clinician can actively control the capsule position and orientation to explore the digestive organs.

Magnetic fields have been widely applied in many applications due to their characteristics [10]–[14]. Among these, wireless actuation of endoscopic capsules has drawn the attention of many biomedical researchers recently. By adding a permanent magnet inside the capsule body and controlling the external magnetic field, one can operate the capsule actively. Several methods have been attempted. Sendoh *et al.* [15] and Chiba *et al.* [16] proposed spiral-shaped capsule endoscopes thrust by rotational and oscillating magnetic fields. Morita *et al.* [17] and Kosa *et al.* [18] developed self-propelling capsule endoscopes with fins that were driven by

Manuscript received October 20, 2018; revised January 29, 2019; accepted May 6, 2019. Date of publication June 12, 2019; date of current version April 15, 2021. This work was supported by the Bio & Medical Technology Development Program of the National Research Foundation (NRF) funded by the Korean Government (MSIT) under Grant 2015M3D5A1065682. This paper was recommended by Associate Editor H.-X. Li. *(Corresponding authors: Byungjeon Kang; Jong-Oh Park; Chang-Sei Kim.)*

M. C. Hoang, K. T. Nguyen, V. H. Le, E. Choi, J.-O. Park, and C.-S. Kim are with the School of Mechanical Engineering, Chonnam National University, Gwangju 61186, South Korea (e-mail: hmcuong.hust@gmail.com; nguyenkimtien90@gmail.com; leviethavn@gmail.com; eunpyochoi@jnu.ac.kr; jop@jnu.ac.kr; ckim@jnu.ac.kr).

J. Kim and B. Kang are with the Medical Actuators Laboratory, Korea Institute of Medical Microrobot, Gwangju 61011, South Korea (e-mail: jaya@jnu.ac.kr; bjkang8204@jnu.ac.kr).

Color versions of one or more figures in this article are available at https://doi.org/10.1109/TSMC.2019.2917298.

Digital Object Identifier 10.1109/TSMC.2019.2917298

a magnetic field. These devices depend on the spiral structure of the capsule and surrounding environment, causing there to be insufficient degrees-of-freedom (DOFs) for the capsule motion.

External robotic devices equipped with a static magnetic attraction field have been studied [19]–[23]. A robotic arm system with a permanent magnet attached to the end effector can move the capsule in the gastrointestinal tract [24]. Carpi *et al.* [25], [26] introduced a Stereotaxis system that used a static magnetic field, and it exhibited good steering performance. These systems incorporated strong magnetic fields from large permanent magnets to control the WCE over obstacles, such as U-shaped folds, but had controllability limitations caused by the one-directional attraction forces from the large external permanent magnets, had insufficient DOFs and a poor response times, and the maneuvering processes were complex.

Recently, electromagnetic actuation (EMA) systems have been applied to WCEs as potential untethered actuators to fulfill multi-DOF motions in the human body. Rey *et al.* [9] and Keller *et al.* [27] presented a magnetic-guided capsule endoscope (MGCE) system to control the capsule in the human stomach. The system consisted of 12 stationary electromagnetic coils and was capable of controlling the capsule with five DOFs, where 2-DOF rotation is used for steering and 3-DOF translation is used for driving the capsule along a desired direction. Lee *et al.* [28] presented an active locomotion intestinal capsule endoscope (ALICE) system for three-dimensional (3-D) locomotion of a WCE in digestive organs. The system consisted of ten coils to generate uniform magnetic fields and gradient magnetic fields separately. The uniform magnetic field generated by a Helmholtz coil and uniform saddle coil were used to align the capsule, and the gradient magnetic field from the saddle pair coils and Maxwell coil was used to propel the capsule along a planned path.

For practical installation at a clinical site, the suggested EMA system configuration must have a maximum available working space within the limited space and a familiar shape with sufficient DOF movability. However, several previous systems could perform head-and-go (HAG) motion only where the propulsion direction was aligned with the heading direction because of the restriction of the electromagnet configuration and the traditional control concept for the magnetic field utilization via the Helmholtz and Maxwell coils. Thus, flexible multi-DOF motion and a large volumetric working space with a minimal system size are essential for untethered capsule endoscope applications, including further micro-functionalities, such as biopsies and tattooing inside the human body [29]–[32] (see Fig. 1).

In this paper, we present a novel method of independent directional steering and driving motion for magnetic actuation of a capsule endoscope (MACE) system for flexible-motion untethered gastrointestinal diagnosis, especially for use in the stomach. This method is a significant improvement, especially in terms of a coil system design for practical medical applications and an independent magnetic field control method, over previous EMA systems applied for microrobot

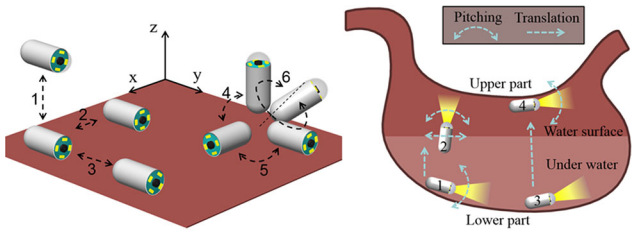

Fig. 1. Motions of a capsule endoscope controlled by the proposed EMA system. (a) Six basic motions of the traditional capsule endoscope: *z*-axis translation, *x*-axis translation, *y*-axis translation, pitching, yawing, and rotation about an arbitrary axis by combining yaw and pitch motion. (b) Newly requested motions for practical diagnosis in the gastrointestinal tract.

actuation [22], [23]. The configuration of the coil system, consisting of eight air-core-type electromagnets, was designed to maximize the inner bore size and minimize the whole EMA system size, which is also related to the weight of the EMA system. The important problem of insufficient force and maneuverability of the capsule was resolved through a novel independent magnetic field control method that utilized a linear combination of magnetic fields. This is significantly different from the previous pair-coil control schemes based on the properties of the Maxwell and Helmholtz coils. Compared to the MGCE [27] (12 coils) and ALICE (10 coils) systems [28], the proposed system uses fewer coils, but can realize 3-D locomotion, regardless of the robot position, with high propulsion force up to 225 mN. Orientation-independent-driving (OID) motions, such as levitation with horizontal alignment, which could not be realized in the previous systems, were demonstrated for conducting scanning tasks more effectively in this paper [see Fig. 1(b)].

The rest of this paper is arranged as follows. In Section II, an overview of the developed system is discussed. The flexible maneuvers, which have not been presented previously, are introduced. The independent control algorithm, together with the remote control scheme, is discussed in Section III. In Section IV, we describe the controllability of the system through the independent control method as well as validation through simulation. The analysis shows that the proposed system is capable of controlling the driving force independently of the capsule's posture. The experimental results described in Section V demonstrate both basic motions and the proposed maneuvers. Section VI concludes this paper and provides a discussion of the proposed system and future work.

II. System Overview

A. MACE Design

The EMA system was designed to have the maximum workspace, accounting for the patient's supine posture and the device's coil size. Fundamental air-core-type electromagnets were incorporated to form the configuration of the EMA system; they could be manufactured at a large scale for clinical applications so that a recumbent patient could be accommodated inside. As illustrated in Fig. 2, the system has a tubular shape with a pair of Helmholtz coils (HC-*y*), a pair

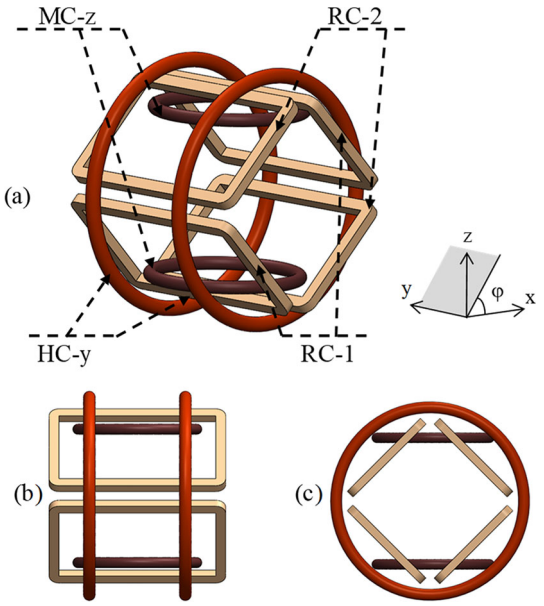

Fig. 2. Schematic of coil configuration of the proposed system. (a) Isometric view. (b) Side view. (c) Front view. HC, MC, and RC denote Helmholtz, Maxwell, and rectangular coils, respectively.

TABLE II
TECHNICAL SPECIFICATIONS OF MACE

Coils	*HC-y*	*MC-z*	*RC-1,2*
Radius (mm)	195	100	n/a
Width × Length (mm)	n/a	n/a	156 × 337
Distance (mm)	195	173.20	200
Diameter of wire (mm)	1.6	1.3	1.3
Number of turns	710	660	600

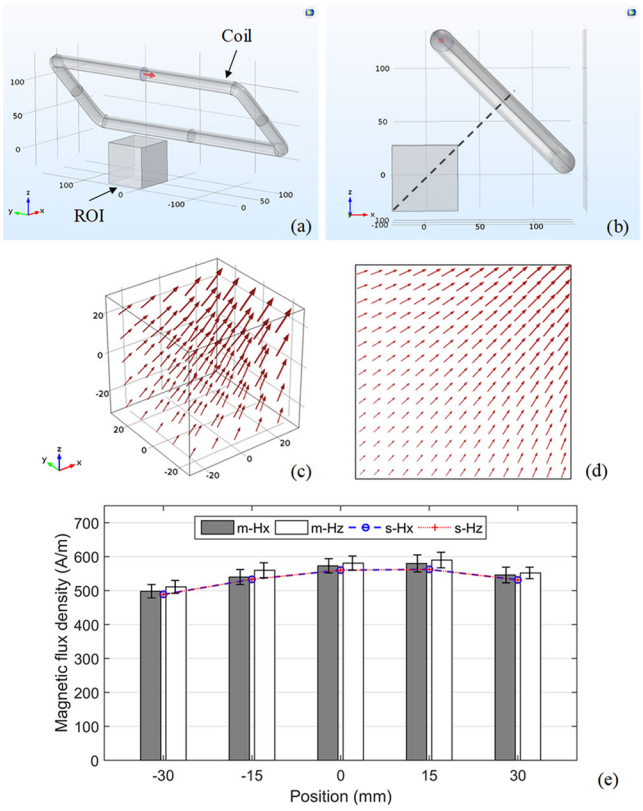

Fig. 3. (a) and (b) FEM model of a rectangular coil with general isometric and *xz*-plane views, respectively. The red arrow indicates the direction of the input current. (c) 3-D magnetic field flux density at 1 A in an ROI of $60 \times 60 \times 60$ (mm^3). (d) Magnetic field map in the *xz*-plane going through the origin in the ROI. The arrows in (c) and (d) indicate the direction and magnitude of the magnetic field. (e) Measured and simulated values of magnetic field intensity in the *x*- and *z*-direction (*m*-Hx, *m*-Hz, *s*-Hx, and *x*-Hz, respectively) at different positions along the *x*- and *z*-axes.

of Maxwell coils (MC-*z*), and two pairs of rectangular coils (RC-1, RC-2). The design specifications of the electromagnetic coils for the prototype EMA system in this paper are summarized in Table II.

To maximize the inner space for the given coil shape and size, we structured the rectangular coils to have 45° inclination angles from the *xy*-plane, as shown in Fig. 2(c), which could accommodate the dorsal length of the human body in a real application. This novel configuration also overcomes the limitation in control of the previous systems, in which only HAG could be achieved. By rotating the RCs 45°, we realized the benefits of the magnetic field in the *x*- and *z*-directions, which enabled the proposed OID motions of the capsule endoscope. Fig. 3 shows the finite element method (FEM) simulation result for the rectangular coil. The normalized magnetic field flux density in the *xz*-plane, as depicted in Fig. 3(d), can be decomposed to magnetic field components in the *x*-direction (*Hx*) and *z*-direction (*Hz*). Fig. 3(e) indicates that *Hx* and *Hz* are approximate and nonuniform magnetic fields contributing magnetic force in the *x*- and *z*-direction to the system.

Inspired by clinically available medical devices, such as magnetic resonance imaging systems and the fundamentals of air-core electromagnets, we applied a similar design concept to our untethered microrobot system. Traditionally, the EMA system has been controlled by utilizing the magnetic field definition of Maxwell and the Helmholtz pair coils, where the gradient magnetic field is created by the Maxwell coil and the uniform magnetic field is created by the Helmholtz coil. However, to enhance the magnetic field and implement more flexible movement, we explored independent magnetic field control on the designed EMA configuration.

B. Motions of the Capsule Endoscope and Special Maneuvers

The basic motions of the capsule, as illustrated in Fig. 1(a), were primarily developed to visualize the digestive organs, which are different in size and shape. The capsule can be controlled to move in the *x*-, *y*-, and *z*-directions and perform pitching and yawing motions [large steering-wheel motion at the head of the capsule, denoted by the numbers 4 and 5 in Fig. 1(a)]. Coupling motions were also required; for example, in narrow tubular-shaped organs, such as the bowel, rotational motion about an arbitrary axis [small steering-wheel motion at the head of the capsule, denoted by the number 6 in Fig. 1(a)] is more effective. The steering-wheel movements of the capsule head (camera position) provide the clinician multiple view angles, which are highly important in endoscopy. Because the miniature camera equipped on the WCE has a limited focusing range, the target cannot be seen clearly when the capsule

is far from the target or too close to the organ's wall [1]; it is even worse for observation of the upper part of the stomach because of the organ's large volume. Hence, additional maneuvers are necessary to manipulate the capsule more easily and effectively in large organs. Fig. 1(b) shows two special scenarios to examine and interact with the upper part of the stomach by OID control. For an application where the organ is filled with water, the capsule can be levitated from position 1 to 2 and maneuvered by translation and pitching at the water surface. However, in cases where the physician needs to interact with tissue, such as in a biopsy, the capsule can levitate from position 3 to 4 and perform pitching motion to create the desired torque. These maneuvers offer the WCE flexibility in diagnosis and eliminate blind spots during large-organ diagnosis.

III. Independent Magnetic Field Control

A. Independently Controlled Electromagnet

When a dipole magnetic object within a microrobot (the endoscopic capsule in this paper) is placed in a magnetic field region (EMA system), it can be aligned and propelled by the magnetic field flux density and gradient magnetic field, respectively. The magnetic torque and force exerted on the microrobot and its equation of motion considering it to be a permanent magnet in the magnetic field region can be expressed as follows:

$$\begin{aligned} \boldsymbol{\tau} &= V\mathbf{M} \times \mathbf{B} \\ \mathbf{F} &= V(\mathbf{M} \bullet \nabla)\mathbf{B} \end{aligned} \tag{1}$$

and

$$M(q)\,\ddot{q} + G(q) + f_{\text{tissue}} + f_{\text{mc}} = \begin{bmatrix} \boldsymbol{\tau} & \mathbf{F} \end{bmatrix}^T \tag{2}$$

where V, $\mathbf{M}$, and $\mathbf{B}$ are the volume and magnetization of the permanent magnet in the WCE and the magnetic field flux density exerted by the EMA system, respectively. M and G are the inertia and gravity of the capsule dynamics, respectively; $q(q = x, y, z)$ is a base coordinate in Cartesian space. f_{tissue} and f_{mc} are friction forces in each direction and muscular contraction forces of the organs, respectively. For *in-vitro* experiments, we discarded the muscular contraction forces [33]. However, muscular contraction and other physiological movements should be considered for *in-vivo* application in the future work. The magnetization of the permanent magnet and the magnetic flux density are described in the Cartesian coordinate system as the following vectors:

$$\mathbf{M} = \begin{bmatrix} M_x, M_y, M_z \end{bmatrix}^T \text{ and } \mathbf{B} = \begin{bmatrix} B_x, B_y, B_z \end{bmatrix}^T. \tag{3}$$

The magnetic torque, $\boldsymbol{\tau}$, changes the orientation of the magnetic object coincident with the direction of the applied magnetic field, $\mathbf{B}$, and the magnetic force, $\mathbf{F}$, drives the microrobot in (1). If the applied magnetic field is not changed too rapidly and the working environment has lower friction, the microrobot will naturally follow the generated magnetic field. However, while manipulating the capsule endoscope in a tissue environment, the resultant magnetic torque must overcome the friction force between the organ's surface and the capsule body. To calculate the magnetic torque, the actual posture of the capsule should be identified, which requires feedback. Hence, to simplify the control, we assume that the WCE always follows the applied external magnetic field and that we needed only a force control strategy. Once the desired motion of the capsule is input to the control system, the controller generates a sufficient magnetic field for the aligning torque and driving force until the actual movement of the capsule occurs so that the operator can control the diagnostic view from a monitor. The driving force can be expressed in a more intuitive form as follows:

$$\mathbf{F} = V\begin{bmatrix} \frac{\partial \mathbf{B}}{\partial x} & \frac{\partial \mathbf{B}}{\partial y} & \frac{\partial \mathbf{B}}{\partial z} \end{bmatrix}^T \mathbf{M}. \tag{4}$$

In addition, for any given point $P(x, y, z)$ in the workspace, the magnetic field created by the nth single electromagnetic coil can be expressed by the vector $\mathbf{B}_n(P)$, which is computed by the product of the input current i in amperes and magnetic field per unit current $\hat{b}_n(P)$ as follows:

$$\mathbf{B}_n(P) = \begin{bmatrix} \mathbf{B}_{x,n}(P) \\ \mathbf{B}_{y,n}(P) \\ \mathbf{B}_{z,n}(P) \end{bmatrix} = \begin{bmatrix} \hat{b}_{x,n}(P) \\ \hat{b}_{y,n}(P) \\ \hat{b}_{z,n}(P) \end{bmatrix} i. \tag{5}$$

Based on the superposition property of the air-core electromagnet, for n-coil system the resultant magnetic field at point P can be expressed by a combination of linearly independent magnetic field vectors as follows:

$$\mathbf{B}(P) = \begin{bmatrix} \hat{b}_{x,1}(P) & \dots & \hat{b}_{x,8}(P) \\ \hat{b}_{y,1}(P) & \dots & \hat{b}_{y,8}(P) \\ \hat{b}_{z,1}(P) & \dots & \hat{b}_{z,8}(P) \end{bmatrix} \begin{bmatrix} i_1 \\ i_2 \\ \vdots \\ i_8 \end{bmatrix} = \hat{\mathbf{b}}(P)\,\mathbf{i} \tag{6}$$

where we considered the eight-coil system designed in this paper. $\hat{\mathbf{b}}(P) \in R^{3\times 8}$ is the mapping matrix in tesla per ampere from the current-input matrix to the magnetic field.

We obtained the partial derivative of the magnetic field, $\mathbf{B}$, along with the x-, y-, and z-directions to compute the magnetic force in (4) in the same manner. These terms can be expressed as the contribution of each individual coil at the center of the workspace

$$\frac{\partial \mathbf{B}(P)}{\partial q} = \begin{bmatrix} \frac{\partial \hat{\mathbf{b}}_1(P)}{\partial q} & \cdots & \frac{\partial \hat{\mathbf{b}}_8(P)}{\partial q} \end{bmatrix} \begin{bmatrix} i_1 \\ i_2 \\ \vdots \\ i_8 \end{bmatrix} = \frac{\partial \hat{\mathbf{b}}(P)}{\partial q}\mathbf{i}. \tag{7}$$

By equating (4), (6), and (7), the resultant magnetic field and magnetic force acting on the unit volume object can be calculated as follows:

$$\begin{bmatrix} \mathbf{B} \\ \mathbf{F} \end{bmatrix} = \begin{bmatrix} \hat{\mathbf{b}}(P) \\ \mathbf{M}^T \partial \hat{\mathbf{b}}(P)/\partial x \\ \mathbf{M}^T \partial \hat{\mathbf{b}}(P)/\partial y \\ \mathbf{M}^T \partial \hat{\mathbf{b}}(P)/\partial z \end{bmatrix} \begin{bmatrix} i_1 \\ i_2 \\ \vdots \\ i_8 \end{bmatrix} = \mathbf{X}(P)\mathbf{i}. \tag{8}$$

Finally, the current inputs to eight electromagnetic coils are mapped onto the magnetic field and force through the 6×8 actuation matrix, $\mathbf{X}(P)$, in (8). Several methods are available to obtain $\hat{\mathbf{b}}(P)$ and $\partial \hat{\mathbf{b}}(P)/\partial q$, which are required to form the actuation matrix for solving the magnetic field and force

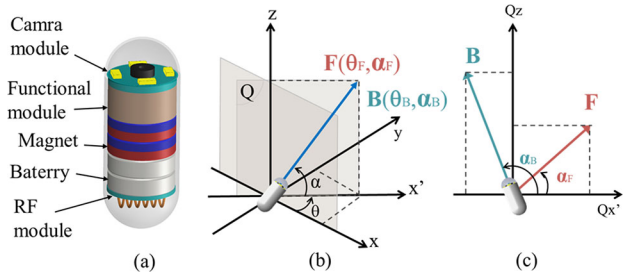

Fig. 4. (a) Capsule endoscope schematic. (b) Remote actuation mechanism of the microrobot. θ defines the angle between the xz-plane and desired plane where the robot is controlled. α represents the angle between the controlled vector and its projection on the xy-plane. (c) OID motion within controlled plane Q.

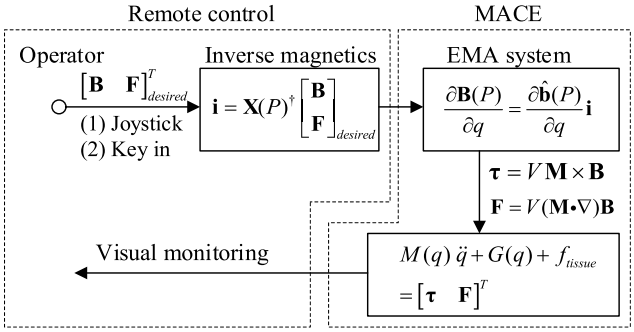

Fig. 5. Block diagram of the remote independent magnetic field control scheme applied to the WCE driven by the external EMA system.

equations of (8). One can either compute the magnetic field values at the center point by the Biot–Savart law, using FEM, or by utilizing actual measurements of the magnetic field of the fabricated system with available magnetic sensors. In this paper, we used the FEM modeling approach to establish the actuation matrix.

Once the desired magnetic field and force, in terms of magnitude and direction, are determined with respect to the operator commands, the input current to each electromagnet can be calculated by using the pseudoinverse of $\mathbf{X}(P)$ as follows:

$$\mathbf{i} = \mathbf{X}(P)^{\dagger} \begin{bmatrix} \mathbf{B} \\ \mathbf{F} \end{bmatrix}_{\text{desired}} \tag{9}$$

where the superscript † denotes the pseudoinverse. Because $\mathbf{X}(P) \in R^{6\times 8}$ is not a symmetric matrix, we choose a two-norm minimized solution as a control input current in (9). The two-norm optimization provided the minimum total input current to all the eight coils, which proportionally minimizes the power consumption and heating issues during EMA operation [34].

B. Remote Control Scheme

The proposed EMA system is designed to control the next generation of capsule endoscopes equipped a functional module, as illustrated in Fig. 4(a). An endoscopic capsule normally has a camera module that takes images of the surrounding environment. The captured images are then sent wirelessly to an external storage device by a radio-frequency module. These electrical components are powered by cell batteries. An untethered capsule with a permanent magnet inside enables remote control. Fig. 4(b) shows the remote actuation scheme with defined magnetic field and force vectors in a global coordinate system for the traditional HAG motion. The vectors' directions are defined by a yaw angle θ and pitch angle α, both of which are applied for the aligning and driving directions. In other words, the capsule can be aligned by the pitch angle α_B within the θ_B-tilted plane Q and driven along the heading direction. Fig. 4(c) illustrates the control scheme for the OID motion, where the WCE can move along any direction without changing its posture, which enables special maneuvers in Fig. 1(b). From the operator input values (the aligning pitch angle α_B, aligning yaw angle θ_B, driving pitch angle α_F, driving yaw angle θ_F, the magnitude of the desired magnetic field $\mathbf{B}$, and the magnitude of magnetic force $\mathbf{F}$), the desired magnetic field and force vectors can be obtained as follows:

$$\begin{bmatrix} \mathbf{B} \\ \mathbf{F} \end{bmatrix}_{\text{desired}} = \begin{bmatrix} B\cos(\alpha_B)\cos(\theta_B) \\ B\cos(\alpha_B)\sin(\theta_B) \\ B\sin(\alpha_B) \\ F\cos(\alpha_F)\cos(\theta_F) \\ F\cos(\alpha_F)\sin(\theta_F) \\ F\sin(\alpha_F) \end{bmatrix} \tag{10}$$

where α_B, θ_B, α_F, and θ_F are input by a joystick device, and B and F are adjusted by a computer keyboard. Equation (10) is substituted into (9) to obtain the input current for each electromagnetic coil. Fig. 5 shows the block diagram of the whole control scheme for the MACE. To guarantee the stability and the safety of the EMA system, limit bounds were set in the software, including maximum supply current (20 A), maximum of B (95 mT) and F (225 mN), and input direction (alignment and propulsion angle) as analyzed in Section IV-A.

IV. System Characterization

A. Maneuverability Analysis

The designed EMA system and microrobot are an over-actuated redundant system, as the number of actuators (eight coils) is greater than the number of DOFs of the microrobot (maximum six DOFs). With six electromagnets, failure conditions occur for some inputs $[\mathbf{B}\ \mathbf{F}]^T$ (which are called singularities) and could lead to physical damage of the electromagnets. Over-actuated redundant systems, by virtue of singularities avoidance and enhanced magnetic forces, can afford alternative processes to the clinician and operators in actual applications [34], [35].

The actuation matrix, $\mathbf{X}(P)$, in (8) is the governing equation of the spatial motion of the microrobot driven by the EMA system. Then, we can predetermine the available robot motions of the system by examining the actuation matrix. The rank of the actuation matrix, $\mathbf{X}(P)$, represents the number of independent constraints and is the number of independent motions that can be driven by the current input to each coil, because the rank of a matrix is the smallest number of independent rows or columns. If the actuation matrix has a greater rank, more independent robot motions can be made. However, physically, because the dipole permanent magnet is unable to rotate about its magnetization axis, the maximum DOFs of

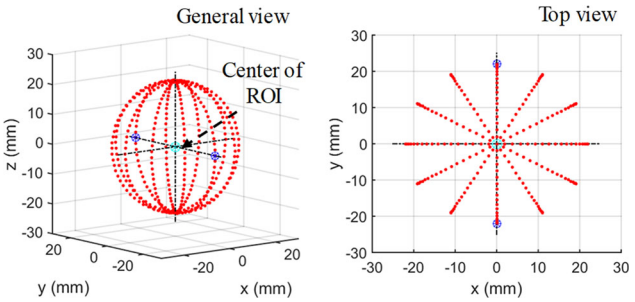

Fig. 6. Rank examination procedure with representative cases. Red dots are the cardinal orientations representing the microrobot postures.

a microrobot having a dipole magnet inside is five, corresponding to x-, y-, and z-translational, yawing, and pitching motions. Thus, the maximum rank of the actuation matrix of the MACE is five.

1) Steering Analysis: It was assumed that the microrobot naturally follows the generated magnetic field in the system's region of interest (ROI). Therefore, the degrees-of-steering of the microrobot are equivalent to those of the EMA system, which is determined by the upper three rows of the actuation matrix, $\hat{\mathbf{b}}(P)$. Using the *rank* function in MATLAB, $\hat{\mathbf{b}}(P)$ has rank 3, which gives the MACE two degrees-of-steering (yawing and pitching motion).

2) Driving Analysis: The magnetic force is determined by the three lower rows of the actuation matrix, which depend on the magnetization $\mathbf{M}$ (posture of the capsule) and magnetic field. Fig. 6 illustrates the representative cardinal orientations of the microrobot postures, corresponding to the available driving directions for the different postures of the robot, where pitch angle α and yaw angle θ vary from 0° to 360°, ignoring overlap. There are three possible rank cases: rank = 1, 2, and 3. Out of the 129.600 posture examinations, two postures have rank 1, as depicted by blue circles in Fig. 6. However, the full DOF motion implementation requires at least rank 2. Thus, we must include exception handling in the control software to avoid singular motion in this case. With $\theta = 0°$, the lower three submatrices have rank 2, and the WCE can be propelled in any direction within the xz-plane, regardless of the alignment direction. For the other postures, we can verify that the rank of the actuation matrix of the system is 3, and the microrobot has full controllability in 3-D space.

B. Simulation: HAG and OID Motion Verification

To verify the independent control theory in which the generated magnetic field is a linear combination of component magnetic fields from individual electromagnets, an FEM simulation was conducted in COMSOL Multiphysics Modeling 5.2 (COMSOL, Inc., Sweden) for the designed system using the parameters in Table II. The unit current (1 A) was input to each coil to obtain the unit magnetic field vector and gradient field components at the center of the ROI. The magnetic field data set in a 60 mm × 60 mm × 60 mm spatial grid for the ROI center was constructed for the *in situ* simulation. The data collected at each point consisted of the magnetic field per unit current and corresponding gradient field components.

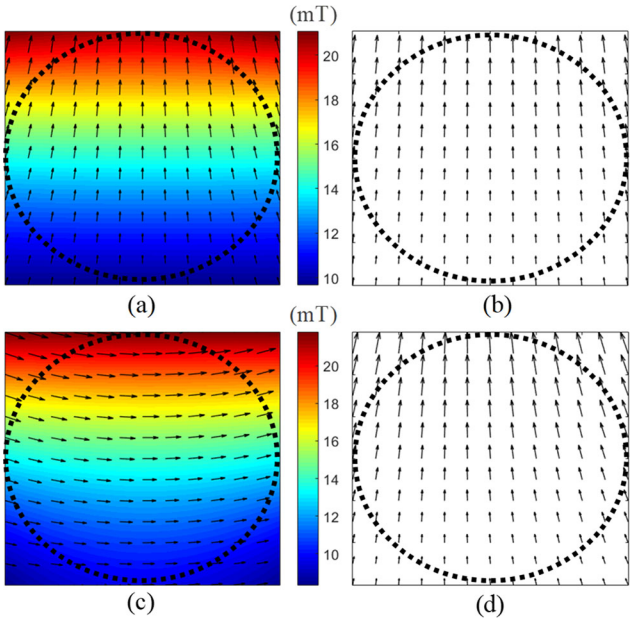

Fig. 7. FEM simulation results in the xz-plane of a 60 mm × 60 mm ROI. The effective ROI is bounded by a black dotted circle. Color indicates the value of the magnetic field. (a) FEM data for HAG control with desired input $(\theta_B, \alpha_B) = (0, 90)$ and $(\theta_F, \alpha_F) = (0, 90)$. (b) Magnetic force map corresponding to (a). (c) FEM data for independent control with desired input $(\theta_B, \alpha_B) = (0, 0)$ and $(\theta_F, \alpha_F) = (0, 90)$. (d) Magnetic force direction corresponding to (c).

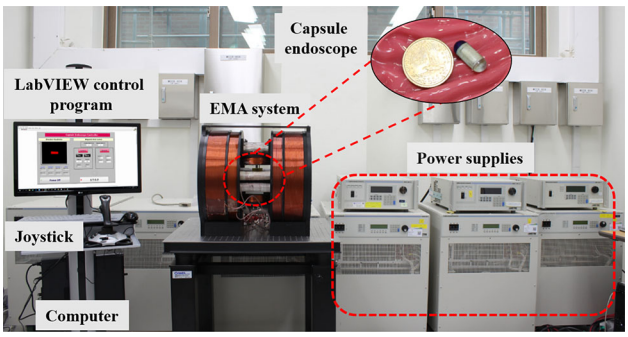

Fig. 8. Experimental setup for the capsule test.

The generated magnetic field at each point were calculated with the current input obtained in (9) by the linearity and superposition property of the magnetic field. Fig. 7 shows the *in situ* simulation results for two representative cases of both control approaches: 1) conventional control (HAG motion) and 2) independent control (OID motion). In the conventional control approach, the WCE is aligned and propelled along the aligned axis [Fig. 7(a) and (b)]. By applying independent control, we could implement OID motion, where the capsule could be levitated with a horizontal posture, as shown in Fig. 7(c) and (d).

V. Experimental Results

A. Experimental Setup

A prototype of the MACE system was built based on the system design concept presented in Section II for performance evaluation. The body frame of the EMA system was made of

TABLE III
CALIBRATION AT THE CENTER POINT OF THE ROI WITH A UNIT CURRENT FOR EACH ELECTROMAGNET

Coil	HC-y,1	HC-y,2	RC-1,1	RC-1,2	RC-2,1	RC-2,2	MC-z,1	MC-z,2
$\mathbf{H}_{\text{simulated}}$ (A/m)	$\begin{bmatrix}0\\1328\\0\end{bmatrix}$	$\begin{bmatrix}0\\1328\\0\end{bmatrix}$	$\begin{bmatrix}548\\0\\548\end{bmatrix}$	$\begin{bmatrix}548\\0\\548\end{bmatrix}$	$\begin{bmatrix}-548\\0\\548\end{bmatrix}$	$\begin{bmatrix}-548\\0\\548\end{bmatrix}$	$\begin{bmatrix}0\\0\\1507\end{bmatrix}$	$\begin{bmatrix}0\\0\\1507\end{bmatrix}$
$\mathbf{H}_{\text{measured}}$ (A/m)	$\begin{bmatrix}13\\1360\\-43\end{bmatrix}$	$\begin{bmatrix}-18\\1330\\-2\end{bmatrix}$	$\begin{bmatrix}573\\-21\\581\end{bmatrix}$	$\begin{bmatrix}556\\36\\598\end{bmatrix}$	$\begin{bmatrix}-548\\13\\554\end{bmatrix}$	$\begin{bmatrix}-568\\16\\564\end{bmatrix}$	$\begin{bmatrix}51\\-2\\1529\end{bmatrix}$	$\begin{bmatrix}45\\2\\1528\end{bmatrix}$
$k=\frac{\lVert\mathbf{H}_{\text{measured}}\rVert}{\lVert\mathbf{H}_{\text{simulated}}\rVert}$	1.05	1.00	1.11	1.13	1.08	1.07	1.03	1.03
Error_θ (degree)	0.55	-0.78	-2.1	-2.63	1.28	1.61	2.25	2.54
Error_α (degree)	1.81	0.09	-0.38	-1.54	1.52	0.21	1.91	1.69

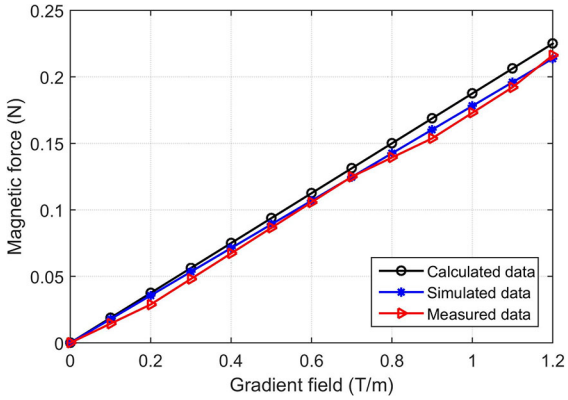

Fig. 9. Simulation and experimental data comparison for a repulsive magnetic force along the y-axis exerted on a capsule, including a cylindrical magnet with a 5-mm diameter and 10-mm length.

aluminum alloy to reduce the high thermal conductivity of the material and lower the sensitivity to the magnetic field. The power supplies of the system were MX12 (4EA) and 3001LX (4EA) from California Instruments, controlled by a LabVIEW program to input the current into each of the eight electromagnets separately. The WCE prototype was fabricated by a 3-D printer, Objet 30 Pro (Stratasys Direct Manufacturing, Ltd., USA) with VeroClear material. A cylindrical permanent magnet made of neodymium (M = 955 000 A/m) with a 5-mm diameter and 10-mm length was placed inside the WCE body. The magnetization direction of the permanent magnet was designed to be aligned with the longitudinal axis of the WCE body. In addition, two cameras (Logitech, C920) were equipped with the EMA system to monitor the motion of the WCE via top and side views. We used a commercially available joystick controller (Logitech, Extreme 3-D Pro) to input the pitch and yaw angles to the system, where the input resolution was set to 1°. The experimental setup is shown in Fig. 8.

B. Calibration

A calibration procedure is necessary to ensure that the generated magnetic field matches that of the simulation.

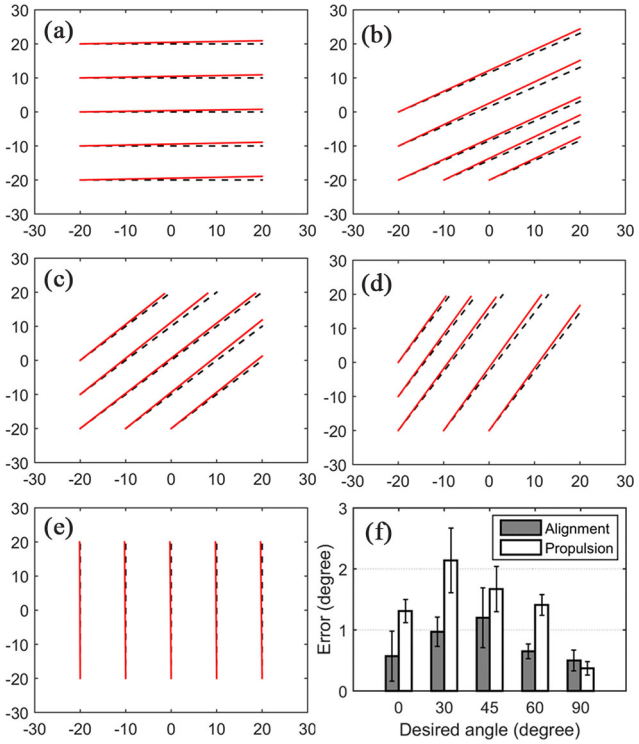

Fig. 10. Tracking error (red solid) for the desired path (black dash) in the xy-plane with the given open-loop control conditions. (a) $\theta = 0°$. (b) $\theta = 30°$. (c) $\theta = 45°$. (d) $\theta = 60°$. (e) $\theta = 90°$. (f) Summary of alignment and propulsion direction errors in the base plane.

To calibrate the MACE, we used a three-channel Bell 8030 Gauss/Tesla meter (Magnetic sciences) to measure the magnetic field $\mathbf{H}$ in amperes per meter at the center of the ROI along x-, y-, and z-axis. A magnetic field was created one-at-a-time by a single electromagnet with an excitation current of 1 A and compared to the simulation values at the ROI's center.

Table III summaries the measured magnetic field $\mathbf{H}_{\text{measured}}$ and simulation field $\mathbf{H}_{\text{simulated}}$. k is the ratio between the magnitudes of the vectors $\mathbf{H}_{\text{measured}}$ and $\mathbf{H}_{\text{simulated}}$. It was used as a scaling factor to generate the magnetic field within the ROI as desired. Error_θ and Error_α were to evaluate the

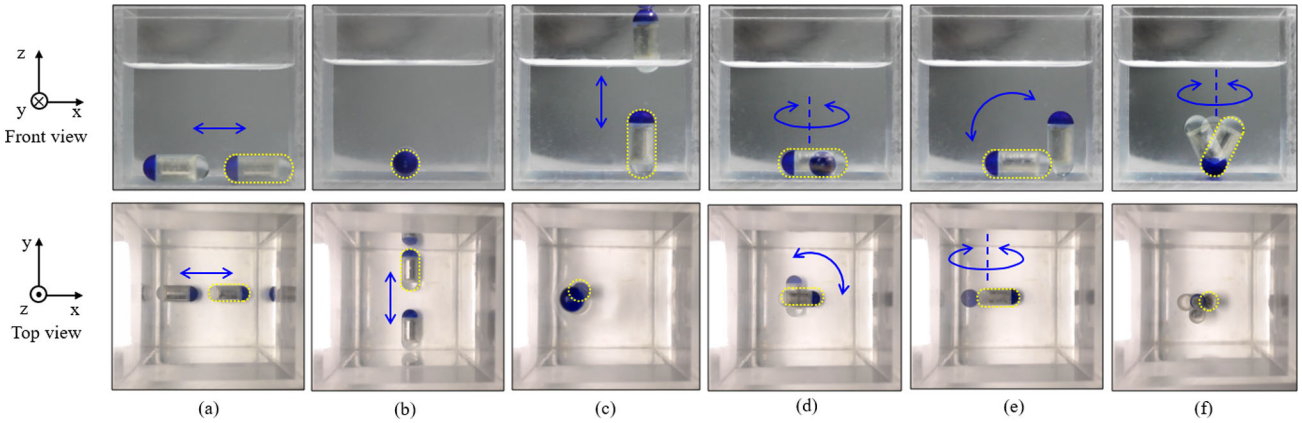

Fig. 11. Overlapping pictures of the HAG control scenario. (a) x-axis translation. (b) y-axis translation. (c) z-axis translation. (d) Yawing. (e) Pitching. (f) Rotation about the z-axis.

misalignment in θ and α directions [see Fig. 4(b)] between the desired (simulation) and real (measured) magnetic field vectors, respectively. They were calculated as follows:

$$\text{Error}_\theta = \tan^{-1}\left(H_{sx}, H_{sy}\right) - \tan^{-1}\left(H_{mx}, H_{my}\right) \quad (11)$$

$$\text{Error}_\alpha = \tan^{-1}\left(\sqrt{H_{sx}^2 + H_{sy}^2}, H_{sz}\right) - \tan^{-1}\left(\sqrt{H_{mx}^2 + H_{my}^2}, H_{mz}\right). \quad (12)$$

The errors were insignificant and remained unchanged when applying the scaling factor to the control software. The coil fabrication process and misalignment during manufacturing of the system were the main error sources.

C. Test of EMA Performance

Fig. 9 shows the magnetic force data of the developed system. To move the capsule in digestive organs, the propulsive or repulsive force from the EMA system must be higher than the frictional force between the capsule and environment, as described in (2). The frictional coefficient was estimated to vary from the order of 10^{-3} in the large intestine to 10^{-1} in the small intestine [25]. This value is dependent on several factors, including the surface properties of the environment, the movement speed, and the geometry of the capsule body [36]–[38]. As suggested in [25], a maximum friction coefficient of 1 is a reasonable value for precautionary. The friction forces exerted on commercial WCEs are estimated to be 30–60 mN depending on their weights [7]. We measured the magnetic force along the y-axis acting on the prototype capsule composed of a permanent magnet with a diameter of 5 mm and a length of 10 mm. To eliminate the effect of the magnetic field, a force gauge (MARK-10 Force Gauge Series 5) was fixed outside the system, and a polymer string was used to connect the capsule and the sensor. The capsule was placed at the center of the ROI inside a glass tube with a diameter of 20 mm along the y-axis. The gradient magnetic field was input from 0 to 1.2 T/m (at maximum supply current) with a step of 0.1 T/m. As shown in Fig. 9, the measured data were close to the calculated and simulated values, and the maximum resultant force was approximately 225 mN, which is approximately four times higher than maximum estimated friction force. From this measurement, one can use the *in situ* force simulation data for quick analysis.

Second, we evaluated the error in the alignment and propulsion directions within the xy-plane. The capsule was placed in a test bed made of an acrylate plate with a size of 60 mm × 60 mm. The bed was filled with silicone oil with a viscosity of 50 cS to avoid the effect of friction and rolling motion due to the cylindrical shape of the capsule's body. The capsule was pushed to move along five representative paths with $\theta = 0°$, 30°, 45°, 60°, and 90°. Each was repeated five times. Fig. 10(a)–(e) shows the reference (desired) and controlled (actual) paths of the examined cases. The errors in the alignment and propulsion directions are summarized in Fig. 10(f). The maximum alignment error was smaller than 1.5° and that of the propulsion angle was approximately 2.7° for the 30° path. In the open-loop control, a small rotational error at the beginning of the motion caused the increase of tracking errors in the movement direction. Ideally, the computational values obtained through the simulation and actual measurements of the electromagnets should be the same. However, because of the physical parameter discrepancy due to fabrication and installation, small propulsion errors were unavoidable. The errors in our system were less than 2.7° within the designed ROI (60 mm × 60 mm) and were insignificant, as discussed elsewhere [28]. For the next step, closed-loop control will be applied to enhance the system's performance.

D. Maneuvering Scenario 1: Head-and-Go Control

Fig. 11 shows overlapping pictures from the top and front views of the six basic motions of the robot illustrated in Fig. 1. HAG control is normally used in the locomotion of a WCE in the gastrointestinal tract because of its simple actuation mechanism, in which the propulsion force is applied along the same direction as the alignment direction. To observe and capture the motions of the capsule during the tests, the capsule was placed in a water-filled transparent cube with a size of 60 mm × 60 mm × 60 mm. For translational motions along the x-, y-, and z-axis, α_F and θ_F were set equal to α_B and θ_B,

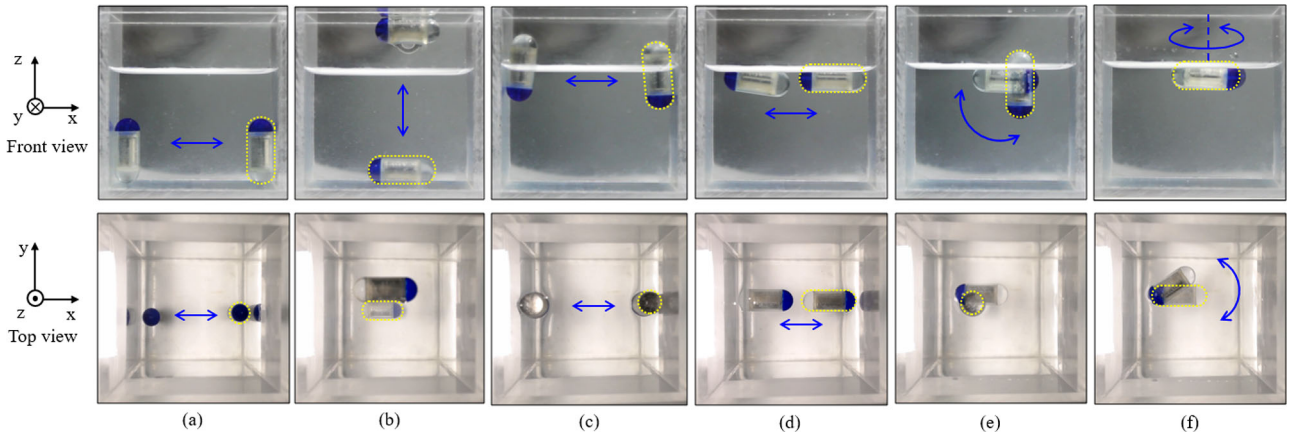

Fig. 12. Overlapping pictures of the OID control scenario. (a) x-translation with z-alignment. (b) z-levitation with x-alignment. (c) x-translation with z-alignment while levitating. (d) x-translation with x-alignment while levitating. (e) Pitching while levitating. (f) Yawing while levitating.

respectively. The gradient field was subsequently created after the alignment to move the capsule along the planned path.

E. Maneuvering Scenario 2: Orientation-Independent-Driving Motion in Water

Unlike HAG control, OID control is proposed for the next generation of WCEs that are capable of not only scanning the digestive organs but also performing functions. When the system has a total rank of 5 or 6, it can be driven in any direction, regardless of the capsule's posture. Fig. 12 illustrates the representative OID movements of the WCE prototype within the xz-plane, in which the propulsion direction and alignment direction were orthogonal. The capsule can be aligned along the z- or x-axis, after which a gradient magnetic field can be applied to move it along x- or z-axis, as shown in Fig. 12(a) and (b), respectively. The capsule could be levitated with a vertical or horizontal posture and moved along the x-axis by slightly changing the propulsion angle, as depicted in Fig. 12(c) and (d). In addition, we demonstrated pitching and yawing motion of the capsule during levitation in Fig. 12(e) and (f), respectively. To do this, the capsule was first lifted at any initial orientation, and the pitch (yaw) angles were subsequently adjusted with a step of 1° to the desired direction.

F. Maneuvering Scenario 3: OID Control in Air

In the case where the capsule works in a stomach not filled with water, it is difficult to lift and maintain its position in air. One can apply OID control to lift the capsule at any initial posture and then perform pitching or yawing to obtain a close-up view of the upper part or general view of the bottom. Fig. 13 shows the pitching motions while levitating the prototype in a stomach-shaped phantom. This OID motion is useful when the operator wants the capsule to interact with the tissue. For a functional WCE, the torque due to the rolling motion while levitating motion can be significant.

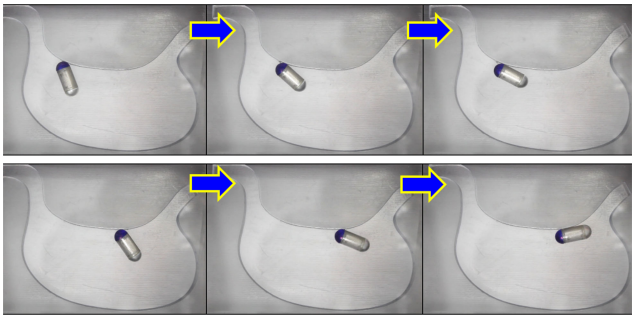

Fig. 13. Independent control (levitation and pitching) to scan the upper part of the stomach at different positions in an air environment.

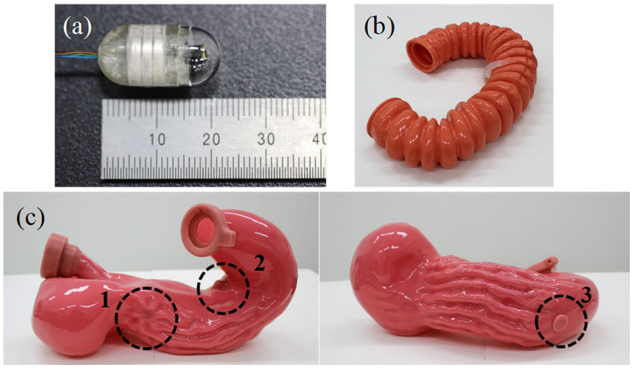

Fig. 14. (a) Capsule endoscope equipped with a wired camera. (b) Large intestine phantom. (c) Stomach phantom with targets: 1—early gastric cancer, 2—gastric ulcers, and 3—polyp.

G. Capsule Endoscope in Stomach Phantom

To evaluate the performance of the proposed system, we conducted experiments in stomach and large intestine phantom from EsophagoGastroDuodenoscopy Simulator LM-103 (see Fig. 14). The capsule was equipped with a small wired camera and permanent magnets. The outer cover of the capsule was fabricated by a 3-D printer, Objet 30 Pro (Stratasys Direct Manufacturing, Ltd., USA), with VeroClear material. The capsule was connected to the center computer via an image acquisition device to store data from the camera. To diagnose the upper part of the stomach without water, we

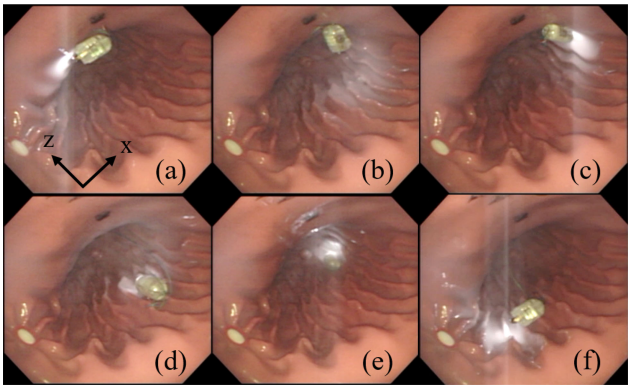

Fig. 15. Captured images of capsule movements in the stomach phantom from endoscopy. (a)–(c) Levitation and pitching. (d)–(f) Locomotion.

applied maneuvering scenario 3 to the capsule. In the stomach phantom, there were two lesions and one polyp. The goal was to search and visualize them for the clinician. The movements of the capsule were observed by a conventional endoscope instrument to evaluate the performance in the stomach phantom. The captured images are shown in Fig. 15. Fig. 16 shows the images extracted from the capsule upon reaching the targets. The MACE demonstrated the ability of the capsule robot to explore the digestive organs.

H. Ex-Vivo Test

The *ex-vivo* test was performed in a piece of porcine small intestine purchased from slaughterhouse. It was not preprocessed to keep the features of real tissue, including viscosity and elasticity. 70 mm of small intestine was collapsed and put in air inside ROI of EMA system as shown in Fig. 17. Capsule was align along *y*-axis and moved forward and backward. Fig. 17 illustrates the sequential images of capsule's movement with estimated average speed of 88 mm/s. Capsule could move straightly as planned with relative high velocity compared to previous discussed studies. This is a significant improvement due to the enhanced magnetic field and propulsion force.

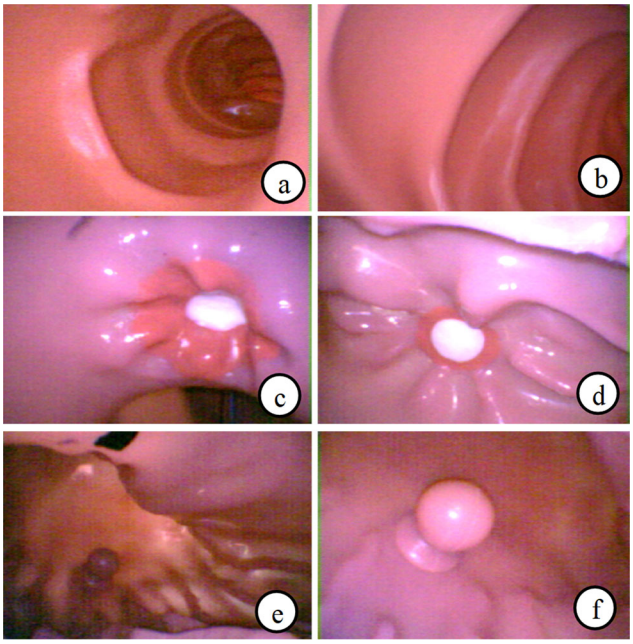

Fig. 16. Captured images from the camera of the WCE in the stomach phantom. (a) General appearance of the large intestine. (b) Close-up view of the large intestine wall. (c) Gastric ulcer-position 2 in Fig. 14(b). (d) Early gastric cancer-position 1 in Fig. 14(b). (e) General view of the lower stomach. (f) Close-up view of polyp-position 3 in Fig. 14(b).

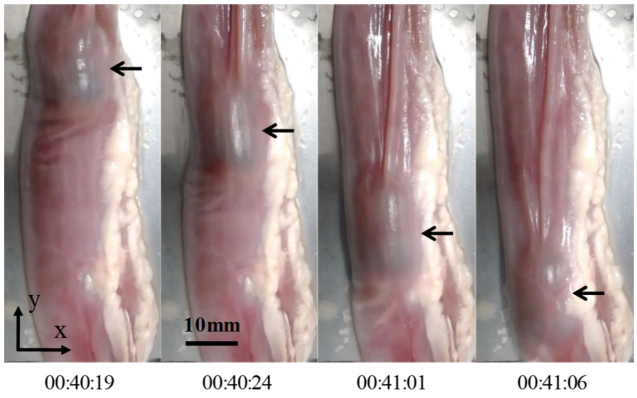

Fig. 17. Movement of capsule in collapsed porcine small intestine with timecode in format min:sec:frame (captured frame rate was 30 frames/s).

VI. Discussion and Conclusion

This paper presented an independent electromagnetic field control method of a novel EMA system for flexible motional manipulation of a capsule endoscope. Table IV summarizes the comparison between the proposed system and previous EMA systems for capsule endoscope applications. The proposed system can generate higher magnetic fields and gradient field with fewer electromagnets. The MACE can perform OID motions, which can overcome the limitations of conventional EMA systems and provide functional flexibility. For example, a WCE can be integrated with a biopsy tool in the middle of the body to sample tissue [26], [39]. For previous systems, the clinician may require the patient to turn around to take sample tissue at the upper parts of the examined organs [9], [22]. With the MACE, a biopsy capsule can be levitated and rolled simultaneously to cut the upper tissue without moving the patient. MACE also has the potential for use in other medical applications, such as magnetically tipped catheters and guidewires.

The MACE system consists of a novel EMA system, a WCE, and an independent magnetic field control methodology. The configuration of the EMA system is designed to realize maximized workspace for a given coil size with eight air-cored electromagnets. Those air-cored electromagnets are conventional coil systems, known as Helmholtz and Maxwell coils that have been previously utilized with a constraint of pair-coil control. Herein, by developing a novel methodology of independent magnetic field control for this conventional coil configuration, we enhanced the ROI of the EMA system and the electromagnetic field strength. As a result, the developed EMA system could realize 5-DOF wireless OID motion control of the WCE and produce up to 225 mN of propulsion force on the capsule prototype.

TABLE IV
COMPARISON OF ELECTROMAGNETIC COIL SYSTEMS FOR CAPSULE ENDOSCOPE MANIPULATION

System [reference]	*MGCE [27]*	*ALICE [28]*	*Proposed system*
Coil configuration	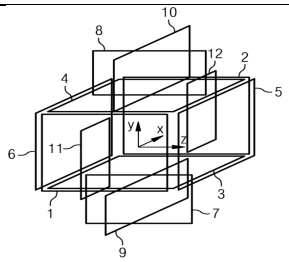	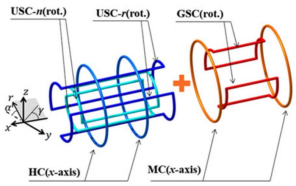	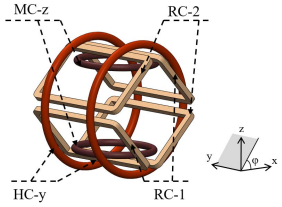
Number of electromagnets	12	10	8
Bore radius	Unknown	195 mm	195 mm
Rotational mechanism	No	Yes	No
Maximum magnetic field	100 mT	46 mT	95 mT
Maximum magnetic force	Unknown	70 mN (cylindrical magnet with 6 mm diameter and 12 mm length)	225 mN (cylindrical magnet with 5 mm diameter and 10 mm length)
OID motion	No	No	Yes

The estimated moving speed in small intestine of pig was 88 mm/s, which is high in applications for capsule and results in shortening the diagnosis time. To the best of the authors' knowledge, this paper is the first to apply independent magnetic field control for the conventional pair coil system, resulting in an enlarged workspace, strengthened magnetic field, and minimized input current. Clinically, compared to other systems, the proposed system can provide superiority for precise diagnosis of gastrointestinal tract through active locomotion as well as short diagnostic time by enhanced electromagnetic field. Optimized system size can be implemented for middle- and small-size clinical environment. In addition, using fewer air-core electromagnet with optimized electrical consumption also brings cost effectiveness for practical implementation.

We also showed a practical application of the independent magnetic field control methodology for special maneuvers of the capsule endoscope with more flexible spatial motions. These maneuvers were demonstrated through simulations and *in-vitro* experiments in a stomach phantom. Through the application of the suggested coil system and control methodology of an endoscopic capsule, the MACE could provide flexible motions of a WCE for further applications. The results demonstrated the high potential for multifunctional applications of the microrobot, such as biopsies, tattooing, and microsurgery in digestive organs, utilizing the developed locomotion modalities and position recognition [40].

Since the MACE is composed of electromagnets that are also considered to be inductors, operating with an alternating current may cause changes in the inductance of the coils. That would result in distortion of the magnetic field due to current attenuation and heat induction effects. However, our system operates with a direct current, then, these factors can be neglected. Generally, EMA systems have a common limitation in heat issue, because operating with a high electrical current for long periods of time leads to increasing temperature of the overall system. A cooling system should be considered for actual full-size systems.

This paper remains several limitations. The experiments were conducted without considering the organic disturbances, such as peristaltic motion of digestive organs and pressures from nearby organs and so on. Since these physiological disturbances are not predictable and can be evaluated by *in-vivo* experiments, future work will be conducted to deal with these unmeasurable quantities based on the enhanced electromagnets utilization proposed in this paper. Moreover, the advanced control and dynamic analysis will be studied for the development of autonomous WCEs, including closed-loop feedback control by utilizing available output measurements. As well, *in-vivo* WCE position estimation methods will also be implemented for precise motion control and unmanned maneuvering by using recently proposed methods [41]–[43].

Finally, the actual scaled system will be fabricated, and *in-vivo* experiments will be conducted based on the proof-of-concept validation results in this paper for practical installation at clinical sites.

REFERENCES

[1] G. Iddan, G. Meron, A. Glukhovsky, and P. Swain, "Wireless capsule endoscopy," *Nature*, vol. 405, pp. 417–418, May 2000.
[2] P. Swain, "The future of wireless capsule endoscopy," *World J. Gastroenterol.*, vol. 14, no. 26, pp. 4142–4145, 2008.
[3] W. A. Qureshi, "Current and future applications of the capsule camera," *Nat. Rev. Drug Disc.*, vol. 3, no. 5, pp. 447–450, 2004.
[4] N. Schoofs, J. Devière, and A. Van Gossum, "PillCam colon capsule endoscopy compared with colonoscopy for colorectal tumor diagnosis: A prospective pilot study," *Endoscopy*, vol. 38, no. 10, pp. 971–977, 2006.
[5] A. Mussetto *et al.*, "MiroCam^{TM} capsule for obscure gastrointestinal bleeding: A prospective, single centre experience," *Dig. Liver Dis.*, vol. 45, no. 2, pp. 124–128, 2013.
[6] Z. Liao *et al.*, "Fields of applications, diagnostic yields and findings of OMOM capsule endoscopy in 2400 Chinese patients," *World J. Gastroenterol.*, vol. 16, no. 21, pp. 2669–2676, 2010.
[7] P. Valdastri, M. Simi, and R. J. Webster, III, "Advanced technologies for gastrointestinal endoscopy," *Annu. Rev. Biomed. Eng.*, vol. 14, pp. 397–429, May 2012.
[8] Z. Liao, R. Gao, C. Xu, and Z. S. Li, "Indications and detection, completion, and retention rates of small-bowel capsule endoscopy: A systematic review," *Gastrointest. Endoscopy*, vol. 71, no. 2, pp. 280–286, 2010.

[9] J. F. Rey *et al.*, "Feasibility of stomach exploration with a guided capsule endoscope," *Endoscopy*, vol. 42, no. 7, pp. 541–545, 2010.
[10] X. Chen, J. Yu, Z. Wu, Y. Meng, and S. Kong, "Toward a maneuverable miniature robotic fish equipped with a novel magnetic actuator system," *IEEE Trans. Syst., Man, Cybern., Syst.*, to be published.
[11] R. Dong, Y. Tan, and Q. Tan, "Mirror angle tuning of electromagnetic micro-mirrors with oscillation compensation," *IEEE Trans. Syst., Man, Cybern., Syst.*, to be published.
[12] Q. Cao, Y. Tan, R. Dong, and W. Shen, "A modeling method of electromagnetic micromirror in random noisy environment," *IEEE Trans. Syst., Man, Cybern., Syst.*, to be published.
[13] W. Lv, Y. Kang, and J. Qin, "Indoor localization for skid-steering mobile robot by fusing encoder, gyroscope, and magnetometer," *IEEE Trans. Syst., Man, Cybern., Syst.*, vol. 49, no. 6, pp. 1241–1253, Jun. 2019.
[14] S. Zihajehzadeh and E. J. Park, "A novel biomechanical model-aided IMU/UWB fusion for magnetometer-free lower body motion capture," *IEEE Trans. Syst., Man, Cybern., Syst.*, vol. 47, no. 6, pp. 927–938, Jun. 2017.
[15] M. Sendoh, K. Ishiyama, and K.-I. Arai, "Fabrication of magnetic actuator for use in a capsule endoscope," *IEEE Trans. Magn.*, vol. 39, no. 5, pp. 3232–3234, Sep. 2003.
[16] A. Chiba *et al.*, "Magnetic actuator for a capsule endoscope navigation system," *J. Magn.*, vol. 12, no. 2, pp. 89–92, 2007.
[17] E. Morita *et al.*, "*In vivo* trial of a driving system for a self-propelling capsule endoscope using a magnetic field (with video)," *Gastrointest. Endoscopy*, vol. 72, no. 4, pp. 836–840, 2010.
[18] G. Kosa, P. Jakab, F. Jolesz, and N. Hata, "Swimming capsule endoscope using static and RF magnetic field of MRI for propulsion," in *Proc. IEEE Int. Conf. Robot. Autom.*, 2008, pp. 2922–2927.
[19] G. Ciuti *et al.*, "Robotic versus manual control in magnetic steering of an endoscopic capsule," *Endoscopy*, vol. 42, no. 2, pp. 148–152, 2010.
[20] G. Ciuti *et al.*, "A comparative evaluation of control interfaces for a robotic-aided endoscopic capsule platform," *IEEE Trans. Robot.*, vol. 28, no. 2, pp. 534–538, Apr. 2012.
[21] S. Yim and M. Sitti, "Design and rolling locomotion of a magnetically actuated soft capsule endoscope," *IEEE Trans. Robot.*, vol. 28, no. 1, pp. 183–194, Feb. 2012.
[22] A. W. Mahoney and J. J. Abbott, "Five-degree-of-freedom manipulation of an untethered magnetic device in fluid using a single permanent magnet with application in stomach capsule endoscopy," *Int. J. Robot. Res.*, vol. 35, nos. 1–3, pp. 129–147, 2016.
[23] G. Ciuti, P. Valdastri, A. Menciassi, and P. Dario, "Robotic magnetic steering and locomotion of capsule endoscope for diagnostic and surgical endoluminal procedures," *Robotica*, vol. 28, no. 2, pp. 199–207, 2010.
[24] A. W. Mahoney and J. J. Abbott, "Generating rotating magnetic fields with a single permanent magnet for propulsion of untethered magnetic devices in a lumen," *IEEE Trans. Robot.*, vol. 30, no. 2, pp. 411–420, Apr. 2014.
[25] F. Carpi and C. Pappone, "Magnetic maneuvering of endoscopic capsules by means of a robotic navigation system," *IEEE Trans. Biomed. Eng.*, vol. 56, no. 5, pp. 1482–1490, May 2009.
[26] F. Carpi, N. Kastelein, M. Talcott, and C. Pappone, "Magnetically controllable gastrointestinal steering of video capsules," *IEEE Trans. Biomed. Eng.*, vol. 58, no. 2, pp. 231–234, Feb. 2011.
[27] H. Keller *et al.*, "Method for navigation and control of a magnetically guided capsule endoscope in the human stomach," in *Proc. 4th IEEE RAS/EMBS Int. Conf. Biomed. Robot. Biomechatronics*, Rome, Italy, 2012, pp. 859–865.
[28] C. Lee *et al.*, "Active locomotive intestinal capsule endoscope (ALICE) system: A prospective feasibility study," *IEEE/ASME Trans. Mechatronics*, vol. 20, no. 5, pp. 2067–2074, Oct. 2015.
[29] J. L. Gorlewicz *et al.*, "Wireless insufflation of the gastrointestinal tract," *IEEE Trans. Biomed. Eng.*, vol. 60, no. 5, pp. 1225–1233, May 2013.
[30] V. H. Le *et al.*, "A soft-magnet-based drug-delivery module for active locomotive intestinal capsule endoscopy using an electromagnetic actuation system," *Sensors Actuators A Phys.*, vol. 243, pp. 81–89, 2016.
[31] V. H. Le *et al.*, "Electromagnetic field intensity triggered micro-biopsy device for active locomotive capsule endoscope," *Mechatronics*, vol. 36, pp. 112–118, Jun. 2016.
[32] G. Go, V. D. Nguyen, Z. Jin, J.-O. Park, and S. Park, "A thermo-electromagnetically actuated microrobot for the targeted transport of therapeutic agents," *Int. J. Control. Autom. Syst.*, vol. 16, no. 3, pp. 1341–1354, 2018.
[33] B. S. Terry, A. B. Lyle, J. A. Schoen, and M. E. Rentschler, "Preliminary mechanical characterization of the small bowel for *in vivo* robotic mobility," *J. Biomech. Eng.*, vol. 133, no. 9, 2011, Art. no. 091010.
[34] J.-P. Merlet, "Redundant parallel manipulators," *Lab. Robot. Autom.*, vol. 8, no. 1, pp. 17–24, 1996.
[35] B. Dasgupta and T. S. Mruthyunjaya, "Force redundancy in parallel manipulators: Theoretical and practical issues," *Mechanism Mach. Theory*, vol. 33, no. 6, pp. 727–742, 1998.
[36] N.-K. Baek, I.-H. Sung, and D.-E. Kim, "Frictional resistance characteristics of a capsule inside the intestine for microendoscope design," *Proc. Inst. Mech. Eng. H J. Eng. Med.*, vol. 218, no. 3, pp. 193–201, 2004.
[37] V. I. Egorov, I. V. Schastlivtsev, E. V. Prut, A. O. Baranov, and R. A. Turusov, "Mechanical properties of the human gastrointestinal tract," *J. Biomech.*, vol. 35, no. 10, pp. 1417–1425, 2002.
[38] D. Accoto *et al.*, "Measurements of the frictional properties of the gastrointestinal tract," in *Proc. World Tribol. Congr.*, vol. 3, no. 7, 2001, p. 728.
[39] V. H. Le *et al.*, "Shape memory alloy-based biopsy device for active locomotive intestinal capsule endoscope," *Proc. Inst. Mech. Eng. H J. Eng. Med.*, vol. 229, no. 3, pp. 255–263, 2015.
[40] T. D. Than, G. Alici, H. Zhou, S. Harvey, and W. Li, "Enhanced localization of robotic capsule endoscopes using positron emission markers and rigid-body transformation," *IEEE Trans. Syst., Man, Cybern., Syst.*, vol. 49, no. 6, pp. 1270–1284, Jun. 2019.
[41] P. B. Nguyen *et al.*, "Real-time microrobot posture recognition via biplane *X*-ray imaging system for external electromagnetic actuation," *Int. J. Comput. Assist. Radiol. Surg.*, vol. 13, no. 11, pp. 1843–1852, 2018.
[42] J. Back and W. Ha, "Robust tracking of robot manipulators via momentum-based disturbance observer and passivity-based controller," *Int. J. Control. Autom. Syst.*, vol. 17, no. 4, pp. 976–985, 2019.
[43] D. Son, S. Yim, and M. Sitti, "A 5-D localization method for a magnetically manipulated untethered robot using a 2-D array of hall-effect sensors," *IEEE/ASME Trans. Mechatronics*, vol. 21, no. 2, pp. 708–716, Apr. 2016.

Manh Cuong Hoang received the B.S. degree in automation control from the School of Electrical Engineering, Hanoi University of Science and Technology, Hanoi, Vietnam, in 2016. He is currently pursuing the Ph.D. degree in mechanical engineering with Chonnam National University, Gwangju, South Korea.

He is a Researcher with the Medical Microrobot Center, Chonnam National University. His current research interests include medical microrobot manipulation and biomedical applications.

Kim Tien Nguyen received the B.S. degree in mechanical engineering from the Ho Chi Minh University of Technology and Education, Ho Chi Minh City, Vietnam, in 2012 and the M.S. degree in mechanical engineering from Chonnam National University, Gwangju, South Korea, in 2015, where he is currently pursuing the Ph.D. degree in mechanical engineering.

He is a Researcher with the Medical Microrobot Center, Chonnam National University. His current research interests include micro-actuator/robot and micromanipulation for biomedical devices/applications.

Viet Ha Le received the B.S. degree in mechanical engineering from the Hanoi University of Science and Technology, Hanoi, Vietnam, in 2013 and the Ph.D. degree in mechanical engineering from Chonnam National University, Gwangju, South Korea, in 2019.

From 2013 to 2019, he was a Guest Researcher with the Medical Microrobot Center, Chonnam National University. He is currently a Researcher with Korea Advanced Materials Institute, Seoul, South Korea. His current research interests include microrobot, microactuator, medical robot, and material for additive manufacturing process.

Jayoung Kim received the B.S. degree in mechanical engineering from Chungbuk National University, Cheongju, South Korea, in 2008, and the M.S. degree in mechanical engineering and the Ph.D. degree in mechatronics engineering from Chungnam National University, Daejeon, South Korea, in 2011 and 2018, respectively.

He is currently a Senior Researcher with the Medical Actuators Laboratory, Korea Institute of Medical Microrobot, Gwangju, South Korea. His current research interests include AI-based prediction, dynamic mechanisms, and control systems for micro-/macro-robots.

Eunpyo Choi received the B.S., M.S., and Ph.D. degrees in mechanical engineering from Sogang University, Seoul, South Korea, in 2008, 2010, and 2015, respectively.

He was a Senior Post-Doctoral Fellow with the Department of Bioengineering, University of Washington, Seattle, WA, USA. He is currently an Assistant Professor with the School of Mechanical Engineering, Chonnam National University, Gwangju, South Korea. His current research interests include BioMEMS and micro/nanorobots for medical approaches.

Byungjeon Kang received the B.S. and M.S. degrees in mechanical engineering from Chonnam National University, Gwangju, South Korea, in 2008 and 2010, respectively, and the Ph.D. degree in biorobotics from Scuola Superiore Sant'Anna, Pisa, Italy, in 2015.

He is currently a Senior Researcher with the Medical Actuators Laboratory, Korea Institute of Medical Microrobot, Gwangju. His current research interests include microactuator/robot and micromanipulation for biomedical applications.

Jong-Oh Park (M'09) received the B.S. degree in mechanical engineering from Yonsei University, Seoul, South Korea, in 1978, the M.S. degree in mechanical engineering from the Korea Advanced Institute of Advanced Technology, Daejeon, South Korea, in 1981, and the Ph.D. degree in robotics from Stuttgart University, Stuttgart, Germany, in 1987.

From 1982 to 1987, he was a Guest Researcher with the Fraunhofer-Institut für Produktionstechnik und Automatisierung, Stuttgart. He was a Principal Researcher with the Korea Institute of Science and Technology, Seoul, from 1987 to 2005, where he was the Director of the Microsystem Research Center from 1999 to 2005. In 2005, he moved to Chonnam National University, Gwangju, South Korea, where he is currently a Full Professor with the School of Mechanical Engineering and the Director of the Robot Research Initiative. His current research interests include biomedical microrobots, medical robots, and service robots.

Chang-Sei Kim (M'14) received the B.S. degree in control and mechanical engineering from Pusan National University, Busan, South Korea, in 1998, the M.S. degree in mechanical engineering from the Department of Mechanical Design and Production Engineering, Seoul National University, Seoul, South Korea, in 2000, and the Ph.D. degree in mechanical engineering from Pusan National University, in 2011.

He was a Research Associate with the Department of Mechanical Engineering, University of Maryland at College Park, College Park, MD, USA. He is currently an Assistant Professor with the School of Mechanical Engineering, Chonnam National University, Gwangju, South Korea. His current research interests include dynamics and control applications for mechanical and biomedical systems in the real world.